Airborne remote sensing of ocean wave directional wavenumber spectra in the marginal ice zone

Peter Sutherland[1] and **Jean-Claude Gascard[2]**

[1]Laboratoire d'Océanographie Physique et Spatiale, L'Institut Français de Recherche pour l'Exploitation de la Mer, Plouzané, France, [2]Laboratoire d'Océanographie et du Climat, Université Pierre et Marie Curie, Paris, France

Abstract Interactions between surface waves and sea ice are thought to be an important, but poorly understood, physical process in the atmosphere-ice-ocean system. In this work, airborne scanning lidar was used to observe ocean waves propagating into the marginal ice zone (MIZ). These represent the first direct spatial measurements of the surface wavefield in the polar MIZ. Data were compared against two attenuation models, one based on viscous dissipation and one based on scattering. Both models were capable of reproducing the measured wave energy. The observed wavenumber dependence of attenuation was found to be consistent with viscous processes, while the spectral spreading of higher wavenumbers suggested a scattering mechanism. Both models reproduced a change in peak direction due to preferential directional filtering. Floe sizes were recorded using colocated visible imagery, and their distribution was found to be consistent with ice breakup by the wavefield.

1. Introduction

Surface waves are known to break up sea ice over large areas [*Liu and Mollo-Christensen*, 1988; *Asplin et al.*, 2012; *Meylan et al.*, 2014; *Collins et al.*, 2015] and also affect ice formation [*Wadhams et al.*, 1987; *Doble et al.*, 2003]. Surface wave propagation in the marginal ice zone (MIZ) — the partially ice covered region at the edge of the sea ice pack, where open ocean processes remain dynamically significant — has been studied since the 1960s [*Robin*, 1963; *Wadhams*, 1973]. The vast majority of theoretical work has focused on the scattering mechanism [e.g., *Squire et al.*, 1995; *Squire*, 2007; *Kohout and Meylan*, 2008]. These models vary widely from models of solitary floating disks [*Meylan and Squire*, 1996] to the comprehensive spectral model of *Masson and Leblond* [1989]. Other authors have treated sea ice as a thin layer of viscous fluid floating on the surface [e.g., *Weber*, 1987; *Liu and Mollo-Christensen*, 1988; *Liu et al.*, 1991]. Recent work has also attempted to merge scattering and viscous models [*Kohout et al.*, 2011]. Scattering and dissipative mechanisms have differing implications for the shape of the transmitted wave spectra; the scattering mechanism suggests that wave spectra at some wavenumbers should broaden, possibly to isotropy, whereas dissipation does not. Thus, the directional spreading of the spectrum of a wavefield entering the MIZ is an important parameter that is both diagnostic of the relevant physical processes and prognostic of the breakup of sea ice.

Field measurements of wave propagation in sea ice have traditionally been quite sparse in comparison to the number of proposed models [*Bennetts et al.*, 2010]. This is largely due to the tremendous technical difficulties involved in making such measurements. The current standard technique is to use wave buoys, either ice mounted or floating, equipped with either tilt sensors or accelerometers [e.g., *Wadhams et al.*, 1988; *Doble et al.*, 2006]. These buoys measure time series of buoy motion, from which Fourier coefficients of the wave directional frequency spectra can be derived [*Steele et al.*, 1985]. Acoustic Doppler current profilers mounted on subsurface moorings or autonomous underwater vehicles have also been successful at extracting the surface wavefield [*Hayes et al.*, 2007]. All of the aforementioned techniques are temporal measurements at a single location; however, in the context of ice breakup, spatial measurements represent a more fundamental quantity.

Satellite and airborne synthetic aperture radar (SAR) imagery have been used to make spatial measurements of ocean swell, both in open water [*Collard et al.*, 2005] and in sea ice [*Lyzenga et al.*, 1985; *Liu et al.*, 1991; *Schulz-Stellenfleth and Lehner*, 2002]. Recent work by *Ardhuin et al.* [2015] has shown Sentinel-1 provides improved swell estimates, particularly in cases with multimodal wave spectra. However, they note that significant uncertainties remain in estimates of directional bias and spreading.
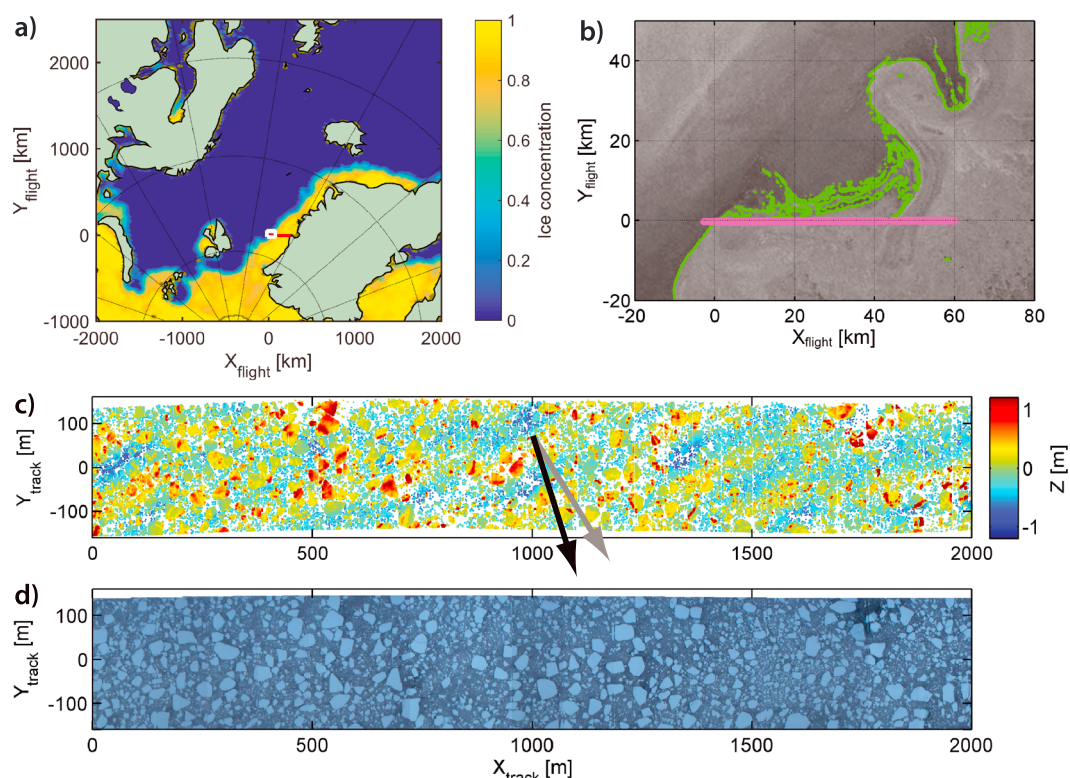
Figure 1. Location of experiment. (a) The large-scale context of the flight path (red line). Land is colored light green, and the background shading shows sea ice concentration [*Cavalieri et al.*, 1999] for the day 30 April 2006 (UTC). The small white box indicates the area shown in Figure 1b. (b) Flight path relative to SAR imagery of sea ice. The gray scale background is wide-swath mode imagery from the ASAR instrument aboard Envisat, taken at 30 April 2006 12:14 UTC. The green line indicates the boundary between the open water and the MIZ. Sea ice is the generally lighter region on the right side of the image; open water is the darker region on the left. The pink line indicates the aircraft flight path. The aircraft flew in the negative X_{flight} direction. (c) Sample airborne lidar surface elevation corresponding to 2 km of data, starting at 32 km along the flight path. Each point corresponds to the location of an individual lidar pulse return, and the color corresponds to the elevation of that point. The black arrow indicates the approximate direction of propagation of the dominant waves corrected for Doppler shifting, and the gray arrow indicates the uncorrected direction. The alternating high/low stripes orthogonal to that direction are the peaks/troughs of individual waves. (d) Color image mosaic over the same area 2 km of flight path, taken by the downward looking camera.

Other than the work of *Campbell et al.* [2014], who used stereo imaging to study wave propagation through floating ice at a lake shore, there have been, to the best of our knowledge, no previous direct measurements of directional wavenumber spectra in the MIZ.

In this work, a new technique, using airborne scanning lidar, has been developed for measurement of the surface wavefield in the MIZ. While single-point airborne lidar systems have been deployed [e.g., *Wadhams*, 1975; *Asplin et al.*, 2012], such measurements are severely limited by the lack of directional information. Scanning lidar has previously been used to study directional wave evolution in open water [*Hwang et al.*, 2000; *Romero and Melville*, 2010] and coastal regions [*Reineman et al.*, 2009; *Huang et al.*, 2012], and was adapted here for use in the MIZ.

2. Measurements

The measurements used in this work were taken by the Geodynamics group at the National Space Institute, Technical University of Denmark, as part of the CryoSat Validation Experiment 2006. The measurement platform was a specially outfitted DHC-6 Twin Otter aircraft. The flight path discussed here is an approximately 60 km transect between 77.57°N, 10.73°W and 77.75°N, 8.18°W (Figure 1a). This path gradually converged with the local ice edge at distances between 0 and 20 km (Figure 1b) and, at 210 km/h, took approximately 17 min to complete.

Stenseng et al. [2007] provide a thorough description of the data collected and the processing techniques. The primary instrumentation was a Riegl Q240i near-infrared lidar scanning in the cross-track direction with a 10 KHz sample rate and 40 Hz scan rate. The ground swath width was approximately equal to the flight altitude, which in this case averaged approximately 400 m. Resulting optimal point spacing was then 1.6 m in both along and across-track directions. Supporting these measurements were downward looking photos, covering the lidar track, taken every 2 s with a nominal spatial resolution of approximately 0.6 m. Lidar and imagery data motion correction and georeferencing was based on a medium-grade ring laser gyro inertial navigation system combined with kinematic global positioning system processing. A full description of this processing is available in *Stenseng et al.* [2007]. Examples of the lidar and imagery data are given in Figure 1c and 1d, respectively.

3. Directional Wavenumber Spectra

The 2-D directional wave energy spectrum, $F(\boldsymbol{k})$, is defined such that $\langle\eta^2\rangle=\int F(\boldsymbol{k})\mathrm{d}\boldsymbol{k}$, where η is the surface elevation, $\boldsymbol{k}$ is the horizontal wavenumber vector, and significant wave height is defined $H_s=4\sqrt{\langle\eta^2\rangle}$. The spectrum can be expressed in polar coordinates as $F(k,\theta)$, where $k=|\boldsymbol{k}|$, and θ is the direction of the wavenumber. In this work, the flight track was divided into 4 km sections, and $F(\boldsymbol{k})$ was calculated for each section. The technique for calculating these spectra is described below; the basic steps were as follows. Separate ice floes from open water, spatially bin average elevation measurements from the open water data, interpolate over empty bins, calculate spectra of gridded data, and correct spectra for Doppler shifting.

Due to the highly variable freeboard of ice floes, often with rapid changes in elevation over short spatial scales, large ice floes were not included in the sea surface elevation records. Since the lidar backscatter from the ice floes was found to be much stronger and more consistent than that of open water, it was possible to create a simple algorithm, based on point density and backscatter amplitude, to select and remove large ice floes. All floes with diameters larger than approximately 4 m were removed in this manner.

Each 4 km flight segment was divided into 20 m × 20 m square bins, and the distribution functions of all non-floe data points within each bin were taken. The elevation value assigned to that bin was then set to the lower 10th percentile of that distribution in order to avoid averaging over the peaks of any small floes with high vertical relief. Any bins which lacked data were then filled using linear interpolation from the surrounding points. This step filled in data in the regions where large floes had been removed. The average ice cover fraction during this experiment was 0.17, and the floe size distribution strongly favored small floes and was limited to less than half the peak wavelength (section 4), meaning that interpolation over floes in the valid wavenumber range was relatively rare.

Two-dimensional spectra of the bin-averaged surface elevation were then calculated for 15 separate overlapping 2-D Hanning windows and averaged.

The motion of the aircraft caused the captured surface to be Doppler shifted. That is, waves moving in the same direction as the motion of the aircraft appeared longer than their true length, and waves moving in the direction opposed to the aircraft's appeared shorter. This Doppler shifting is negligible only when the aircraft speed, u_a, is much larger than the phase speeds of the waves of interest, a condition that was not satisfied during these experiments. Corrections for this Doppler shifting have thus been applied to the wavenumber spectra following the technique outlined by *Walsh et al.* [1985]. They noted that the shift in the wavenumber in the direction of the flight path, δk_x can be written as

$$\delta k_x = \frac{\omega}{u_a}, \qquad (1)$$

where angular frequency, ω, is related to the wavenumber k by the linear dispersion relation, $\omega^2 = gk\tanh(kh)$, where g is gravitational acceleration and h is the water depth (approximately 200 m).

If lidar data are taken in two opposing flight directions, the Doppler shift of the wavefield can then be used to eliminate the 180° directional ambiguity otherwise inherent in spatial wave measurements [*Walsh et al.*, 1985].

The end result of the analysis is a directional wavenumber spectrum for each 4 km flight segment. The spectra are valid over a range of approximately $2\pi/300 \leq k \leq 2\pi/50$ rad/m, with the low wavenumber limit being set by the swath width and the upper limit being set by the noise level in the measurements due to interpolation over ice floes. Examples of resulting spectra are shown in Figure 2.
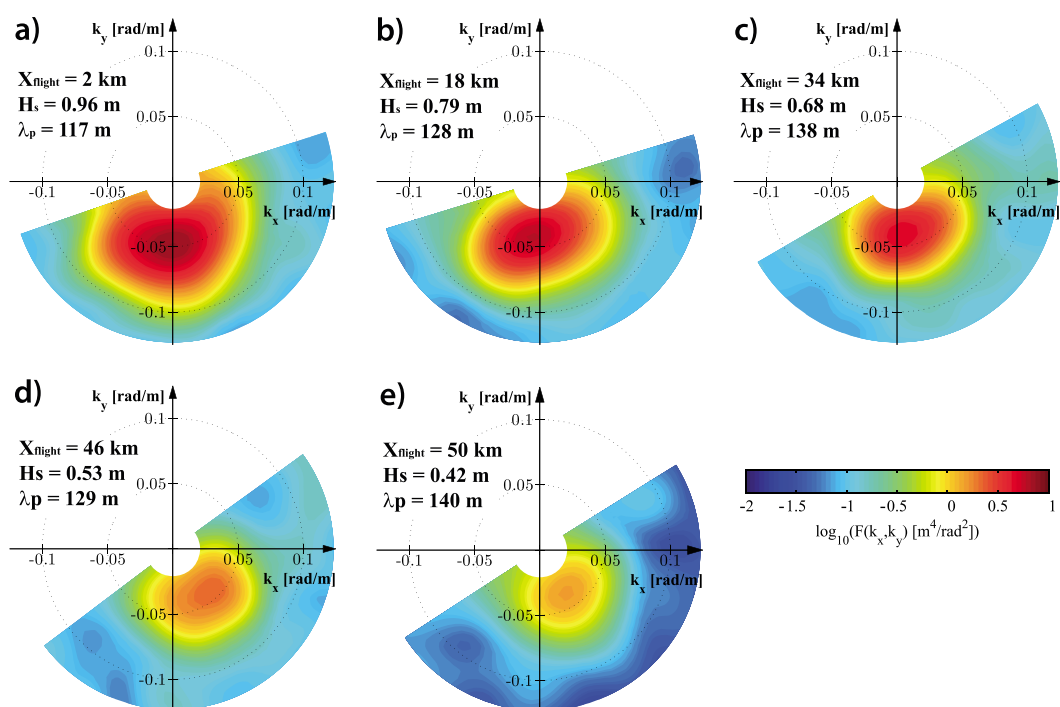
Figure 2. Directional wavenumber spectra of swell propagating through the MIZ. Each panel corresponds to a spectral average over 4 km of flight path. The directions of the axes are in flight path coordinates (cf. Figure 1), and the colors indicate spectral energy. These spectra are subject to a 180° directional ambiguity and so have been clipped to only show the spectra within 90° of the peak incoming wave direction. Along-track locations of each panel are as follows: (a) $X_{flight} = 2$ km. (b) $X_{flight} = 18$ km. (c) $X_{flight} = 34$ km. (d) $X_{flight} = 46$ km. (e) $X_{flight} = 50$ km.

4. Floe Size Distribution

The colocated downward looking visible imagery was used to measure the floe-size distributions. In this work, a threshold-based algorithm was used to detect individual floes. Floe size distributions were taken for both the minor and major axes of floes, over the same 4 km transects as the lidar data, and are shown in Figure 3.

The floe-size distributions appear to follow a truncated power law [e.g., *Lu et al.*, 2008]. The limiting scale of the minor floe axis, L_s, is approximately $L_s < \lambda_p/2$, where $\lambda_p = 2\pi/k_p$ is the peak wavelength (k_p is defined in section 6). The major floe axis also appears to be limited, but by a scale a factor of 2–3 higher. This finding is consistent with the idea that the maximum stress applied to the ice floes is at a scale of approximately
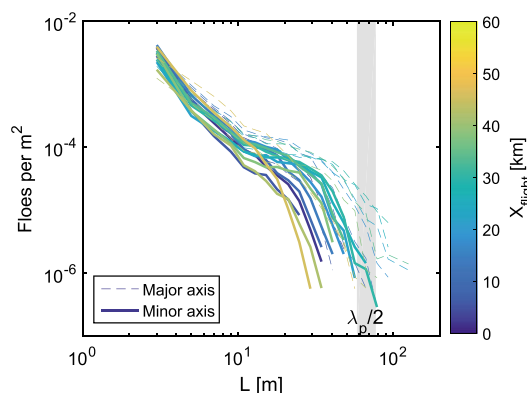
Figure 3. Distributions of floe axis length, L. Each curve corresponds to a 4 km section along the flight path. Solid lines are the distributions of minor axis lengths, L_s, and dashed lines are the distributions of major axis lengths. The shaded gray region denotes the range of observed peak wavelengths, divided by 2. The color scale corresponds to distance along the flight path.

one half the peak wavelength [e.g., *Dumont et al.*, 2011]. That is, floes in the along-wave direction are broken with a scale of $L_s \simeq \lambda/2$, while in the cross-wave direction, they can be somewhat larger, depending on the directional spreading of the spectrum. It should be noted that after the initial breakup, the orientation of the floes is no longer fixed, and they could easily rotate so that their long axis is in the direction of wave propagation and consequently be further broken by the same process.

5. Energy Attenuation

Wave energy per unit area of the sea surface, E, is defined as

$$E = \rho_w g \int_{-\pi}^{\pi} \int_{0}^{\infty} F(k, \theta) k \, d\theta \, dk, \qquad (2)$$

where ρ_w is the water density, and g is gravitational acceleration. This integration was performed for each flight segment.

The literature suggests that wave energy should decay exponentially in the MIZ, with shorter waves being attenuated more rapidly than longer ones [e.g., *Wadhams et al.*, 1988; *Meylan et al.*, 2014]. With an exponential definition of attenuation, and assuming a uniform wavefield and neglecting wind input, non-linear wave-wave interactions, and other dissipation mechanisms, the wave spectral energy at any location, $\boldsymbol{x}$, within the ice can be written as

$$F(\boldsymbol{x}; k, \theta) = F_0(k, \theta) e^{-\alpha(k) X_{ice}(\boldsymbol{x}; \theta)}. \qquad (3)$$

Here $F_0(k, \theta)$ is the incoming wavefield in open water, $F(\boldsymbol{x}; k, \theta)$ is the wave spectrum at position $\boldsymbol{x}$, and $\alpha(k)$ is the wavenumber-dependent attenuation coefficient. The ice fetch, $X_{ice}(\boldsymbol{x}; \theta)$, is a directional function defined such that waves at position $\boldsymbol{x}$, and traveling in direction θ, will have traveled a distance $X_{ice}(\boldsymbol{x}; \theta)$ through the ice from the open water. Ice fetch was estimated using colocated SAR imagery (see supporting information for details). The incoming wavefield was not measured, and so it was instead estimated by using $F(\boldsymbol{x}; k, \theta)$ and $X_{ice}(\boldsymbol{x}; \theta)$ from the flight segment nearest to the open water and then solving equation (3) for $F_0(k, \theta)$.

The formulation of equation (3) was chosen, due to the complex ice front geometry (Figure 1b), because it allows preferential directional filtering; waves that travel farther through the ice are attenuated more than those that take a more direct path from open water. Equation (3) does not directionally redistribute energy. This directional exponential decay was tested using two different models for $\alpha(k)$.

5.1. Viscous Layer Model

Various authors [e.g., *Weber*, 1987; *Liu and Mollo-Christensen*, 1988; *Liu et al.*, 1991] have proposed a treatment of the surface ice layer as a viscous layer. By assuming the ice to behave as a thin ($\tau k \ll 1$, where τ is the ice thickness) layer of highly viscous fluid floating on a less viscous ocean, *Weber* [1987] showed that the attenuation coefficient could be written

$$\alpha(k) = \frac{k^2}{2(\omega/2\nu_{eff})^{1/2}}, \qquad (4)$$

where ν_{eff} is the effective kinematic viscosity in the water. Using the deep water dispersion relation to relate frequency and wavenumber, this can be simplified to

$$\alpha(k) = \frac{\nu_{eff}^{1/2} k^{7/4}}{\sqrt{2} g^{1/4}}. \qquad (5)$$

Effective viscosity, ν_{eff}, in this model is not well quantified. *Weber* [1987] used a value of 4×10^{-4} m²/s, thought to be between ocean interior and turbulent boundary layer values. In this work, we have used a least squares minimization technique to calculate the value of ν_{eff}: For each flight segment, the total wave energy, E, was calculated for both the observed and modeled wavefield; ν_{eff} was then varied to minimize the sum over all flight segments of squared differences between the observed and modeled values of E. Using this methodology, an effective viscosity of $\nu_{eff} = 6.4 \times 10^{-4}$ m²/s was found. This is 1.6 times the value used by *Weber* [1987] and is easily within the range of expected oceanic values [e.g, *Liu et al.*, 1991].

5.2. Scattering Model

Kohout and Meylan [2008] proposed model for wave attenuation based on scattering from multiple floating elastic plates. Viscosity, floe collisions, and nonlinear effects were neglected. They calculated numerical solutions for attenuation rate, *a*, per unit floe number over a range of wave periods and floe thickness. The dimensional attenuation coefficient is then related to *a* by

$$\alpha(k) = C_i \frac{a}{D}, \tag{6}$$

where C_i is ice concentration and D is characteristic floe size [e.g., *Doble and Bidlot*, 2013]. The per-floe, wavenumber-dependent, attenuation coefficient, *a*, is given in Figure 6 of *Kohout and Meylan* [2008] and reproduced in Figure 2 in the supporting information.

Here C_i=0.17 was the mean ice concentration over the entire flight path, and D=30 m was taken from the approximate location of the "bump" observed in the floe size distributions (Figure 3). Direct measurements of ice thickness were not available. However, during the lidar processing, it was possible to calculate the floe freeboard, the elevation of floes above the interpolated floe-free wave surface. The mean freeboard for all floes in the flight was H_{free}=0.34 m. Floe thickness is related to freeboard by

$$\tau = \frac{H_{\text{free}}}{1 - \rho_i/\rho_w}, \tag{7}$$

where ρ_i is ice density. *Timco and Frederking* [1996] give the expected range of densities for multiyear sea ice as ρ_i=720 kg/m³ to ρ_i=910 kg/m³. The lidar measurements cannot distinguish between low-density snow and ice, so for this work a value near the lower end of the expected range, ρ_i = 750 kg/m³, was chosen. Using ρ_w=1035 kg/m³ results in an ice thickness of approximately $\tau = 1.2$ m. The per-floe attenuation coefficient, *a*, was then taken from Figure 6 of *Kohout and Meylan* [2008] for τ=1.2 m, converted from a function of *T* to a function of *k* using the deep water dispersion relation and then applied to equation (6).

6. Discussion

Figure 4 shows modeled wavefield spectral parameters plotted against the measurements for both of the models. For reference, supporting information Figure 3 includes these same quantities, plotted as functions of X_{flight}.

Figure 4a shows total wave energy density, *E*, calculated using equation (2). Unsurprisingly, the viscous [*Weber*, 1987] model fits the data much better than the scattering model [*Kohout and Meylan*, 2008], because least squares regression was used to derive ν_{eff} for the viscous model. The scattering model produced wave energy levels an average of approximately 20% lower than the measurements, which is reasonable considering the previously discussed large uncertainties regarding ice thickness.
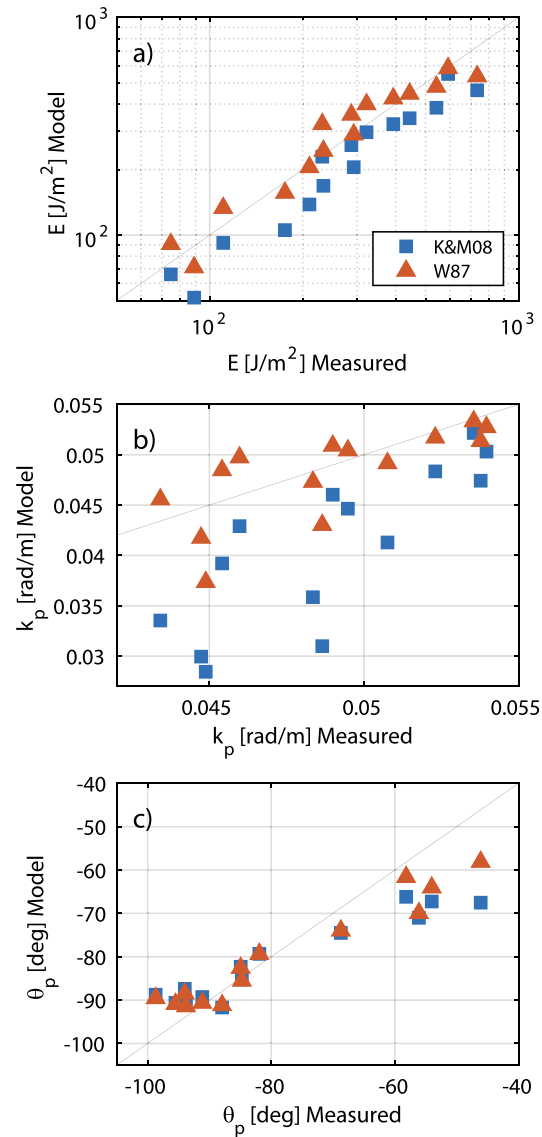
Figure 4b shows wavelength corresponding to the peak of the omnidirectional wavenumber spectrum. The omnidirectional spectrum is defined as

$$\phi(k) = \int_{-\pi}^{\pi} F(k, \theta) k \, \mathrm{d}\theta, \tag{8}$$

and the peak wavenumber, k_p, is the wavenumber where $\phi(k_p) = \max(\phi(k))$. As waves propagate into the ice, higher wavenumbers are attenuated more quickly than lower ones, resulting in a shift of the spectral peak to lower wavenumbers. Consequently, k_p can be used as an indicator of how well a model captures the wavenumber dependence of the attenuation coefficient. Here it is clear that the scattering model underestimates k_p at lower values of k_p (farther from the ice edge). This means that the scattering model attenuates short waves much more quickly than was observed. The viscous model exhibits considerable variability but does not show a bias toward low wavenumbers.

Figure 4c shows the direction of the peak of the spectrum, which was calculated using

$$\theta_p = \frac{\int_{-\pi}^{\pi} \int_{k_a}^{k_b} (F(k, \theta))^q \theta \, \mathrm{d}k \, \mathrm{d}\theta}{\int_{-\pi}^{\pi} \int_{k_a}^{k_b} (F(k, \theta))^q \, \mathrm{d}k \, \mathrm{d}\theta} \tag{9}$$

Figure 4. Comparison of modeled and measured spectral parameters. In all three panels, the abscissæ are the measured values and the ordinates are the modeled values. Each symbol corresponds to a 4 km flight segment. Blue squares are from equation (6), the scattering model of *Kohout and Meylan* [2008], and red triangles are from equation (5), the viscous layer model of *Weber* [1987]. Panel (a) is integrated wave energy from equation (2), (b) is peak wavelength, and (c) is peak wave direction from equation (9).

where $q = 4$ is a constant. Here $k_a = 0.02$ rad/m and $k_b = 0.13$ rad/m are the lower and upper limits of the valid spectral range (see section 3). Peak direction is an indicator of the efficacy of preferential directional filtering. Figure 1b shows that for approximatley $X_{\text{flight}} > 40$ km, waves traveling in a direction of $\theta = -90°$ must traverse far more ice than those traveling in a direction of $\theta = -50°$. The data show a corresponding counterclockwise shift from approximately $\theta_p = -90°$ near the ice edge to $\theta_p = -50°$ in the ice interior. This shift is clearly visible in Figure 2. Both models reproduce this directional shift reasonably well, though they underestimate the turning by 10–20° farther from the ice edge. This additional turning is likely due to refraction by currents, bathymetry, and the ice.

Directional spreading as a function of wavenumber can be written in terms of the wave spectrum as

$$\sigma_\theta(k) = \frac{\int_{-\pi/2}^{\pi/2} F(k, \theta) \left| \theta - \theta_p \right| \mathrm{d}\theta}{\int_{\pi/2}^{\pi/2} F(k, \theta) \mathrm{d}\theta}, \tag{10}$$
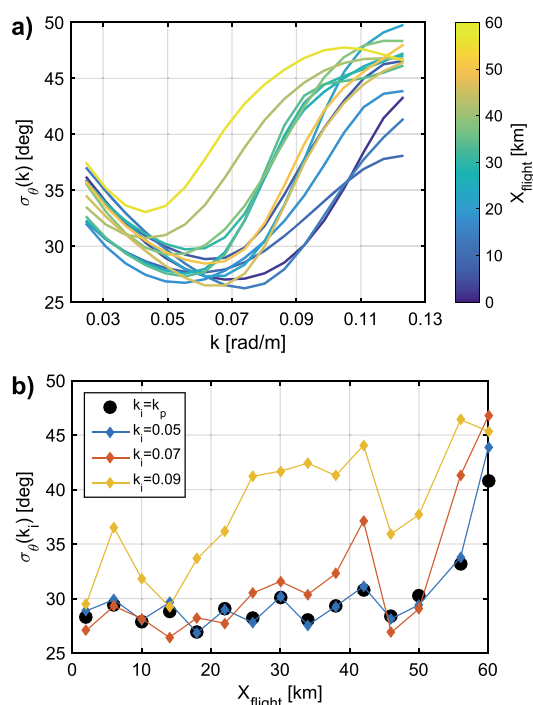
Figure 5. Directional spreading of wavenumber spectra. (a) Spectral spreading, $\sigma_\theta(k)$, as a function of wavenumber (equation (10)). Each curve corresponds to a 4 km flight segment; the color indicates X_{flight}. (b) Spectral spreading at chosen wavenumbers, k_i, as functions of X_{flight}. The black circles are the spreading at $k_i = k_p$, the blue diamonds are at $k_i = 0.05$ rad/m, the red diamonds are at $k_i = 0.07$ rad/m, and the yellow diamonds are at $k_i = 0.09$ rad/m.

and is illustrated in Figure 5a. Figure 5b shows the value of the spreading function at the peak wavenumber and three other wavenumbers, plotted as functions of X_{flight}. The spreading reaches a minimum near k_p, which is expected in open water cases [cf. *Romero and Melville*, 2010]. As the waves propagate farther into the pack, higher wavenumbers display a general trend toward spectral broadening, while spreading at the spectral peak remains approximately constant until approximately $X_{\text{flight}} > 55$ km.

Scattering off of floes is only expected when the wavelength is less than 2–3 times the floe length [*Kohout and Meylan*, 2008]. The observed floe-size distributions (Figure 3), which displayed a cutoff at approximately $L = \lambda_p/2$, then imply that scattering should be minimal at the spectral peak and only become important at higher wavenumbers. This is consistent with the observations of spectral broadening first appearing at the highest wavenumbers.

Since both viscous and spreading models describe some features of the observations — k_p shift, and high wavenumber spreading, respectively — it is likely that both processes are important in the MIZ. In order to disentangle the relevant attenuation mechanisms, a dedicated field campaign, combined with a modeling effort of the type of *Ardhuin et al.* [2016], using a full spectral model, would be expected to provide improved results.

References

Ardhuin, F., F. Collard, B. Chapron, F. Girard-Ardhuin, G. Guitton, A. Mouche, and J. Stopa (2015), Estimates of ocean wave heights and attenuation in sea ice using the SAR wave mode on Sentinel-1a, *Geophys. Res. Lett.*, *42*, 2317–2325, doi:10.1002/2014GL062940.

Ardhuin, F., P. Sutherland, M. Doble, and P. Wadhams (2016), Ocean waves across the arctic: attenuation due to dissipation dominates over scattering for periods longer than 19 s, *Geophys. Res. Lett.*, *43*, doi:10.1002/2016GL068204.

Asplin, M. G., R. Galley, D. G. Barber, and S. Prinsenberg (2012), Fracture of summer perennial sea ice by ocean swell as a result of arctic storms, *J. Geophys. Res.*, *117*, C06025, doi:10.1029/2011JC007221.

Bennetts, L. G., M. A. Peter, V. A. Squire, and M. H. Meylan (2010), A three-dimensional model of wave attenuation in the marginal ice zone, *J. Geophys. Res.*, *115*, C12043, doi:10.1029/2009JC005982.

Campbell, A. J., A. J. Bechle, and C. H. Wu (2014), Observations of surface waves interacting with ice using stereo imaging, *J. Geophys. Res. Oceans*, *119*, 3266–3284, doi:10.1002/2014JC009894.

Cavalieri, D. J., C. L. Parkinson, P. Gloersen, J. C. Comiso, and H. J. Zwally (1999), Deriving long-term time series of sea ice cover from satellite passive-microwave multisensor data sets, *J. Geophys. Res.*, *104*(C7), 15,803–15,814, doi:10.1029/1999JC900081.

Collard, F., F. Ardhuin, and B. Chapron (2005), Extraction of coastal ocean wave fields from sar images, *IEEE J. Oceanic Eng.*, *30*, 526–533, doi:10.1109/JOE.2005.857503.

Collins, C. O., W. E. Rogers, A. Marchenko, and A. V. Babanin (2015), In situ measurements of an energetic wave event in the arctic marginal ice zone, *Geophys. Res. Lett.*, 1863–1870, doi:10.1002/2015GL063063.

Doble, M., D. Mercer, D. Meldrum, and O. Peppe (2006), Wave measurements on sea ice: Developments in instrumentation, *Ann. Glaciol.*, *44*(1), 108–112, doi:10.3189/172756406781811303.

Doble, M. J., and J.-R. Bidlot (2013), Wave buoy measurements at the antarctic sea ice edge compared with an enhanced ECMWF WAM: Progress towards global waves-in-ice modelling, *Ocean Model.*, *70*, 166–173, doi:10.1016/j.ocemod.2013.05.012.

Doble, M. J., M. D. Coon, and P. Wadhams (2003), Pancake ice formation in the Weddell Sea, *J. Geophys. Res.*, *108*, 3209, doi:10.1029/2002JC001373.

Dumont, D., A. Kohout, and L. Bertino (2011), A wave-based model for the marginal ice zone including a floe breaking parameterization, *J. Geophys. Res.*, *116*, C04001, doi:10.1029/2010JC006682.

Hayes, D. R., A. Jenkins, and S. McPhail (2007), Autonomous underwater vehicle measurements of surface wave decay and directional spectra in the marginal sea ice zone, *J. Phys. Oceanogr.*, *37*, 71–83.

Huang, Z.-C., B. D. Reineman, L. Lenain, W. K. Melville, and J. H. Middleton (2012), Airborne lidar measurements of wave energy dissipation in a coral reef lagoon system, *J. Geophys. Res.*, *117*, C03016, doi:10.1029/2011JC007203.

Hwang, P. A., D. W. Wang, E. J. Walsh, W. B. Krabill, and R. N. Swift (2000), Airborne measurements of the wavenumber spectra of ocean surface waves. Part I: Spectral slope and dimensionless spectral coefficient, *J. Phys. Oceanogr.*, *30*(11), 2753–2767.

Kohout, A. L., and M. H. Meylan (2008), An elastic plate model for wave attenuation and ice floe breaking in the marginal ice zone, *J. Geophys. Res.*, *113*, C09016, doi:10.1029/2007JC004434.

Kohout, A. L., M. H. Meylan, and D. R. Plew (2011), Wave attenuation in a marginal ice zone due to the bottom roughness of ice floes, *Ann. Glaciol.*, *52*(57), 118–122.

Liu, A. K., B. Holt, and P. W. Vachon (1991), Wave propagation in the marginal ice zone: Model predictions and comparisons with buoy and synthetic aperture radar data, *J. Geophys. Res.*, *96*(C3), 4605–4621, doi:10.1029/90JC02267.

Liu, A. K., and E. Mollo-Christensen (1988), Wave propagation in a solid ice pack, *J. Phys. Oceanogr.*, *18*, 1702–1712.

Lu, P., Z. J. Li, Z. H. Zhang, and X. L. Dong (2008), Aerial observations of floe size distribution in the marginal ice zone of summer prydz bay, *J. Geophys. Res.*, *113*, C02011, doi:10.1029/2006JC003965.

Lyzenga, D. R., R. A. Shuchman, J. D. Lyden, and C. L. Rufenach (1985), Sar imaging of waves in water and ice: Evidence for velocity bunching, *J. Geophys. Res.*, *90*, 1031–1036.

Masson, D., and P. H. Leblond (1989), Spectral evolution of wind-generated surface gravity waves in a dispersed ice field, *J. Fluid Mech.*, *202*, 43–81, doi:10.1017/S0022112089001096.

Meylan, M. H., and V. A. Squire (1996), Response of a circular ice floe to ocean waves, *J. Geophys. Res.*, *101*(C4), 8869–8884, doi:10.1029/95JC03706.

Meylan, M. H., L. G. Bennetts, and A. L. Kohout (2014), In situ measurements and analysis of ocean waves in the antarctic marginal ice zone, *Geophys. Res. Lett.*, *41*, 5046–5051, doi:10.1002/2014GL060809.

Reineman, B. D., L. Lenain, D. Castel, and W. K. Melville (2009), A portable airborne scanning lidar system for ocean and coastal applications, *J. Atmos. Oceanic Technol.*, *26*, 2626–2641.

Robin, G. D. Q. (1963), Wave propagation through fields of pack ice, *Philos. Trans. R. Soc. London, Ser. A*, *255*, 313–339, doi:10.1098/rsta.1963.0006.

Romero, L., and W. K. Melville (2010), Airborne observations of fetch-limited waves in the Gulf of Tehuantepec, *J. Phys. Oceanogr.*, *40*, 441–465.

Schulz-Stellenfleth, J., and S. Lehner (2002), Spaceborne synthetic aperture radar observations of ocean waves traveling into sea ice, *J. Geophys. Res.*, *C8*, 3106, doi:10.1029/2001JC00837.

Squire, V. (2007), Of ocean waves and sea-ice revisited, *Cold Reg. Sci. Technol.*, *49*(2), 110–133, doi:10.1016/j.coldregions.2007.04.007.

Squire, V. A., J. P. Dugan, P. Wadhams, P. J. Rottier, and A. K. Liu (1995), Of ocean waves and sea ice, *Annu. Rev. Fluid Mech.*, *27*(1), 115–168, doi:10.1146/annurev.fl.27.010195.000555.

Steele, K., J. Lau, and Y.-H. Hsu (1985), Theory and application of calibration techniques for an NDBC directional wave measurements buoy, *IEEE J. Oceanic Eng.*, *10*(4), 382–396, doi:10.1109/JOE.1985.1145116.

Stenseng, L., S. Hvidegaard, H. Skourup, R. Forsberg, C. Andersen, S. Hanson, R. Cullen, and V. Helm (2007), Airborne lidar and radar measurements in and around Greenland CryoVEx, *Tech. Rep.*, Danish National Space Center.

Timco, G., and R. Frederking (1996), A review of sea ice density, *Cold Reg. Sci. Technol.*, *24*(1), 1–6, doi:10.1016/0165-232X(95)00007-X.

Wadhams, P. (1973), Attenuation of swell by sea ice, *J. Geophys. Res.*, *78*(18), 3552–3563, doi:10.1029/JC078i018p03552.

Wadhams, P. (1975), Airborne laser profiling of swell in an open ice field, *J. Geophys. Res.*, *80*(33), 4520–4528, doi:10.1029/JC080i033p04520.

Wadhams, P., M. A. Lange, and S. F. Ackley (1987), The ice thickness distribution across the Atlantic sector of the Antarctic Ocean in midwinter, *J. Geophys. Res.*, *92*(C13), 14,535–14,552, doi:10.1029/JC092iC13p14535.

Wadhams, P., V. A. Squire, D. J. Goodman, A. M. Cowan, and S. C. Moore (1988), The attenuation rates of ocean waves in the marginal ice zone, *J. Geophys. Res.*, *93*(C6), 6799–6818, doi:10.1029/JC093iC06p06799.

Walsh, E. J., D. W. H. III, D. E. Hines, R. N. Swift, and J. F. Scott (1985), Directional wave spectra measured with the surface contour radar, *J. Phys. Oceanogr.*, *15*, 566–592.

Weber, J. E. (1987), Wave drift and wave attenuation in the marginal ice zone, *J. Phys. Oceanogr.*, *17*, 2352–2361.